Contents lists available at ScienceDirect

Applied Catalysis B: Environmental

Improved visible-light photocatalytic activity of NaTaO$_3$ with perovskite-like structure via sulfur anion doping

Fang-Fei Li [a], Da-Rui Liu [b], Gui-Mei Gao [b], Bing Xue [a], Yin-Shan Jiang [a],*

[a] Key Laboratory of Automobile Materials, Ministry of Education, and Department of Materials Science and Engineering, Jilin University, 5988 People's Avenue, Changchun, 130025, PR China
[b] Research & Project Demonstration Center of Comprehensive Utilization of Coal and Associated Resources, Shenhua Zhungeer Energy Resource Comprehensive Development Co. Ltd., Xue Jia Wan Huhhot, 010300, PR China

ARTICLE INFO

ABSTRACT

A novel sulfur anion-doped NaTaO$_3$ photocatalyst with nanocubic morphology, at an average size of 200–500 nm or so, was synthesized by a simple hydrothermal process. The as-prepared samples were characterized by various techniques, such as X-ray diffraction (XRD), X-ray photoelectron spectroscopy (XPS), scanning electron microscopy (SEM), UV–vis diffuse reflectance spectra (UV–vis DRS) and photocatalytic degradation evaluation. The results indicate that the as-prepared NaTaO$_3$ is assigned to monoclinic lattice, which is much closer to cubic phase than conventional orthorhombic perovskite structure. And doping of S anions would cause, to some extent at least, expanded unit cell and distorted lattice structure from monoclinic into cubic phase, whose Ta—O—Ta band angle is much closer to 180°, resulting in the higher mobility of photo induced charge carriers. Narrowed band gap and splitting slopes are observed in S-doped NaTaO$_3$ by UV–vis DRS, confirming the visible-light adsorption capability and the upward shifted valence band edge, which come from the overlapping of S 3p orbitals and Ta 5d orbitals. In virtue of the crystalline and electronic structures, the resultant S-doped NaTaO$_3$ samples, as compared with pure NaTaO$_3$, exhibit remarkably improved visible-light photocatalytic activity and similar UV-light photocatalytic activity, during the photocatalytic degradation of methyl orange. In addition, S-doped NaTaO$_3$ also displays reliable recycling photocatalytic performance and satisfying solar catalytic activity for the organic pollutant. On the basic of above experimental phenomena, a possible mechanism for sulfur anion doping in NaTaO$_3$ perovskite-like structure is also presented.

© 2014 Elsevier B.V. All rights reserved.

1. Introduction

Significant attentions have been paid on ABO$_3$ perovskite-type oxides due to their high performances in photocatalytic reactions, such as overall water splitting and photo degradation of organic pollutants, which provided promising methods to solve our urgent energy and environmental problems [1–9]. Comparing with other kinds of perovskite-like semiconductors, NaTaO$_3$ attracts much attention due to its stable layered structure and excellent separation effectiveness in charge separation, which promotes the efficiency of photoelectrochemical and photocatalytic systems [6,7,9–13].

However, only a small UV fraction of solar irradiation, about 2–3%, can be utilized by NaTaO$_3$ because of its wide band gap

(4 eV or so, depends on the lattice structure [14,15]). Therefore, great efforts have been made to add dopants into NaTaO$_3$, such as Bi, La, Sm, RuO$_2$, LaFeO$_3$, and N etc. [16–28], in order to narrow the band gap and hence improve its utilization for solar beams. Unlike the doped cations which usually reduce the conduction band-edge potential of NaTaO$_3$ [17,29], doped anions at O-sites tend to increase the valence band-edge potential of semiconductors, which is crucial for the properties of photo-induced holes generated at the top of valence band, and leading to varied photocatalytic activities [30,31]. Thus, doping anions into NaTaO$_3$ seems to be a promising method to obtain visible-light photocatalyst with higher performance.

Although N-doped NaTaO$_3$, the pioneer of anion doping attempt in NaTaO$_3$ materials, has displayed remarkable improvement in visible-light photocatalytic activity [24–28,31], experimental reports on other anion-doped or co-doped NaTaO$_3$ systems to date were still limited. The main shortcoming of such N mono-doping system is the generation of excessive holes on the top of valence

band, caused by different valence values between dopant and host elements [30,31]. These undesirable holes are usually concerned as recombination centers for electron-hole trapping, leading to the decay of photocatalytic activity. Among various nonmetallic dopants (such as F, N, C, S, and P), only sulfur has the same valence electrons as oxygen, thus the substitution of S on the O-site would not introduce undesirable holes or defects into $NaTaO_3$. In addition, recent theoretical work carried out by Ahuja group [30] has shown that, similarly to well known S-doped TiO_2 [32–35], S monodoping could shift the valence band edge of $NaTaO_3$ upward with a value of 1.35 eV, and reduce the band gap remarkably, without losing the ability to split water into H_2 and O_2. They also found that, only S-doped $NaTaO_3$ displayed negative minimum formation energy, indicating the most energetically favorable than any other anion monodoping systems. That means S anion doping might endow $NaTaO_3$ with higher photocatalytic activity and better utilization of solar energy. However, experimental researches on S-doped $NaTaO_3$ photocatalyst are very rare. Comparing with N^{3-}, the ionic radius of S^{2-} is much larger, indicating notably different doping effects and doping mechanism from N-doped $NaTaO_3$, which need to be further revealed.

It has been reported that both the lattice structure and the electronic structure of $NaTaO_3$ were sensitive to the synthesis route [10–13]. Solid-state reaction is the conventional technique to obtain $NaTaO_3$, which requires long time high-temperature calcination, typically 1000–1300 °C [1,2,11,19,23,24]. In such circumstance, it's difficult indeed for the doped elements, which have variational valence states, to be preserved in anion states. Further researches have found that, $NaTaO_3$ perovskite could be synthesized by much milder methods and at much lower temperatures [6–13,20–22,26–28,36–38], even at room temperature [38], which provided tremendous possibilities for the experimental attempts of achieving stable anion-monodoped $NaTaO_3$. Among these methods, hydrothermal synthesis is promising for the direct preparation of advanced nanostructures dispensed with calcination procedure [6,7,9,11–13,20,26–28], which is desirable for generating S anion-doped $NaTaO_3$ with highly crystalline structure, narrow size distribution, and low aggregation.

In our previous works [27,28], N^{3-}-doped $NaTaO_3$ has been successfully prepared by hydrothermal method, which exhibited improved visible-light photocatalytic activity. In virtue of similar hydrothermal system, in this article, $Na_2S_2O_3$ is employed to synthesize S anion-doped $NaTaO_3$ nanocubes. In favor of better crystalline formation and less A-site defects of $NaTaO_3$, which is crucial for the activity of photocatalyst, high NaOH concentration is applied for the hydrothermal process [1,2,12,28]. The doping amounts and valence states of S species in the resultant $NaTaO_3$ are detected by XPS analysis. The sulfur doping effects on the microstructure, morphology, and threshold wavelength are investigated to improve the photocatalytic activities of $NaTaO_3$, and a possible mechanism for sulfur anion doping in perovskite-like structure is also presented here. The detailed photocatalytic performances on the resultant S-doped $NaTaO_3$ are studied under UV, visible, and natural solar light irradiation respectively, where methyl orange and phenol are chosen as the target pollutants which are considered as the typical components in industry waste water, in order to evaluate the real application possibility of such novel photocatalyst.

2. Experimental

2.1. Synthesis of S-doped $NaTaO_3$ compounds

All of the reagents were analytical grade and used without further purification. $NaTaO_3$ and S-doped $NaTaO_3$ were prepared

by a simple hydrothermal method. In a typical synthesis procedure, 0.442 g of Ta_2O_5, 1.2 g of NaOH and certain amount of $Na_2S_2O_3 \cdot 5H_2O$ were added into a Teflon-line stainless steel autoclave (50 mL capacity) that filled with water to 80% of the total volume. The autoclave was sealed and put into a preheated oven to perform hydrothermal treatment at 180 °C for 12 h. After hydrothermal processing, the resulting precipitates were collected by centrifugation and washed with deionized water for several times, and then dried at 80 °C for 2 h before further characterization and photocatalytic reaction.

The symbols: Sxx will be labeled hereafter, where xx describes the molar percentages of S:Ta in the precursors. For example, S10 represents the S-doped $NaTaO_3$ whose calculated molar ratio of S:Ta is 10%, where the amount of $Na_2S_2O_3 \cdot 5H_2O$ is 0.0248 g during synthesis. It should be note that only half of the sulfur species in $Na_2S_2O_3$ precursor is in anion state, indicating the S^{2-}:Ta ratio in raw materials is reduced by half, namely 5%.

2.2. Characterization

The X-ray powder diffraction (XRD) patterns, obtained on a Bruke/D8-Advance with Cu Kα radiation (λ = 1.518 Å), were used to identify the phase constitutions in samples. The operation voltage and current were maintained at 40 kV and 40 mA, respectively. A scan rate of 10°/min was applied to record the patterns in the range of 2θ = 10–80°. The morphology and microstructure were observed with scanning electronic microscope (SEM, Philps XL-30). UV–vis DRS was obtained using a UV-3600 UV–vis–NIR spectrophotometer (Shimadzu, Japan). $BaSO_4$ was the reference sample and the spectra were recorded in the range of 200–700 nm. The XPS experiments were performed on the S-doped $NaTaO_3$ compounds with ESCALAB 250 instrument (Thermo, USA). The samples were pressed to from a pellet prior to XPS measurement. The binding energy scale was calibrated with respect to the C1s peak of hydrocarbon contamination fixed at 285.0 eV. The bond vibrations of samples were analyzed by FTIR spectrometer (Nexus 6700, Thermo, USA). The identification of intermediate products in the solution was performed employing a gas chromatography mass spectrometry (GC/MS) system. The GC (Hewlett-Packard 6890) is equipped with an HP-1MS capillary column and interfaced directly to the MS (HP 5973) used as a detector.

2.3. Photocatalytic test

Methyl orange (MO) and phenol were chosen as the target pollutants for photocatalytic activity tests, since they were usually considered as the main components in industry waste water and difficult to degrade, namely azo dyes and phenolic compounds respectively. During the photocatalytic degradation experiments, 10 mg of photocatalyst (S-doped $NaTaO_3$ or pure $NaTaO_3$) was added into 10 mL of MO or phenol aqueous solution, whose initial concentration was 20 mg/L. The reactor was cooled by circulating water, and was placed under various light sources. UV light was luminesced by low pressure mercury lamp (8 W, Philips), which has two irradiation peaks at 254 nm and 185 nm, respectively. And visible light was obtained by high pressure mercury lamp (250 W, Philips) with suitable cutoff filters (λ < 420 nm). The tested visible light illumination intensity at the sample surface is 17800 Lx. Before irradiation, the suspension was kept in the dark for 5 h to ensure the adsorption/desorption equilibrium between the photocatalyst and MO. Photocatalytic performances under real solar irradiation were also detected, considering the differences in wavelength distribution of irradiation between natural and man-made light resources. During solar testing, all of the samples were put into the reactors and were paralleled placed under solar light in a fine day, so that the light intensity could be the same for all samples. The concentration of MO, whose absorption peak appeared at 463 nm,
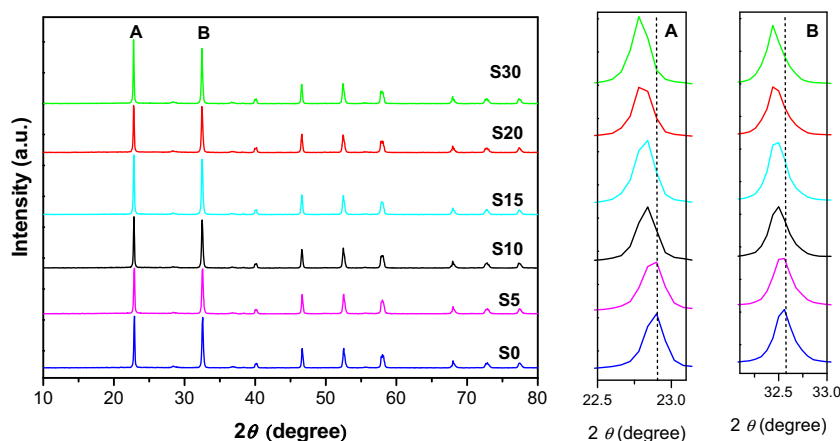
Fig. 1. XRD patterns of S-doped NaTaO$_3$ with various doping amounts.

was monitored by T6 spectrophotometer (Pgeneral, China) at the desired time intervals. No proceeding oxygen was added into the system in order to check the real photocatalytic activity of the samples in usual industrial conditions. The recycling performance of the photocatalyst was carried out as follows: after a certain photocatalytic degradation test, the suspension was centrifugalized, and then the deposition was washed several times followed by drying at 80 °C for 10 h to finish the regeneration process.

The decolorization efficiency was determined by $(1 - A/A_0) \times 100\%$, where A was the observed absorbance value of resultant solution at a certain irradiation time, and A_0 was the initial absorbance value of MO solution. The pseudo-first-order rate constant, k_1, was calculated from the plotting of $\ln(A_0/A)$ versus t, in order to evaluate the activity of photocatalyst.

3. Results and discussion

3.1. Crystal structure.

XRD patterns of S-doped NaTaO$_3$ with various doping amount are shown in Fig. 1. The magnified patterns of two principal peaks (A and B) are also inserted at the right part of Fig. 1. As shown, all of the reflection peaks of the samples can be readily indexed to pure NaTaO$_3$ with a monoclinic structure ($P2/m$ with $a = 3.8936$ Å, $b = 3.8905$ Å, $c = 3.8936$ Å, $\alpha = \gamma = 90°$, and $\beta = 90.267°$; JCPDS 74-2478), which is a familiar product for hydrothermal synthesis method [1,12,36]. As has been reported, perovskite-like NaTaO$_3$ had three polymorphs such as cubic phase, monoclinic phase, and orthorhombic phase. Comparing with conventional

orthorhombic structure where the TaO$_6$ octahedra is twisted, the structure of monoclinic phase is much closer to cubic phase ($Pm3m$ with $a = b = c = 3.929$ Å, $\alpha = \beta = \gamma = 90°$; JCPDS 74-2488), where the connection of TaO$_6$ octahedra is close to an ideal perovskite, implying lower recombination rate for electron-hole pairs [1,11].

A detailed inspection on the magnified principal peaks (shown at the right side of Fig. 1) displays that, with the increase of doping amount of S, the position of the principal peaks shift slightly to lower angle (especially for peak A and Peak B), indicating the tendency of modifying the monoclinic NaTaO$_3$ towards to cubic phase by S doping. Further calculation results also confirm that, as listed in Table 1, with the increasing amount of S, the unit cell volume of NaTaO$_3$ increases slightly, and the angle β tends much close to 90°. It implies that doping with S species leads to gradually structural transition of NaTaO$_3$ from monoclinic phase to cubic phase.

3.2. Morphology analysis

Fig. 2 shows the SEM images of pure NaTaO$_3$ (S0) and S-doped NaTaO$_3$ powders (S20). Both of the two samples are well-crystallized in nanocubic shape, with an average size of 200–500 nm and the exposed crystal faces are considered to be (1 0 0) and (1 1 0) facets [38]. It is a typical morphology for hydrothermal synthesized NaTaO$_3$ [11,12,37], where the nuclei can grow freely in aqueous solution (which is an open space) to form nanocrystals according to their natural crystallographic growth habits. Moreover, doping of S species dose not display obvious variations to the micro-morphology of NaTaO$_3$.
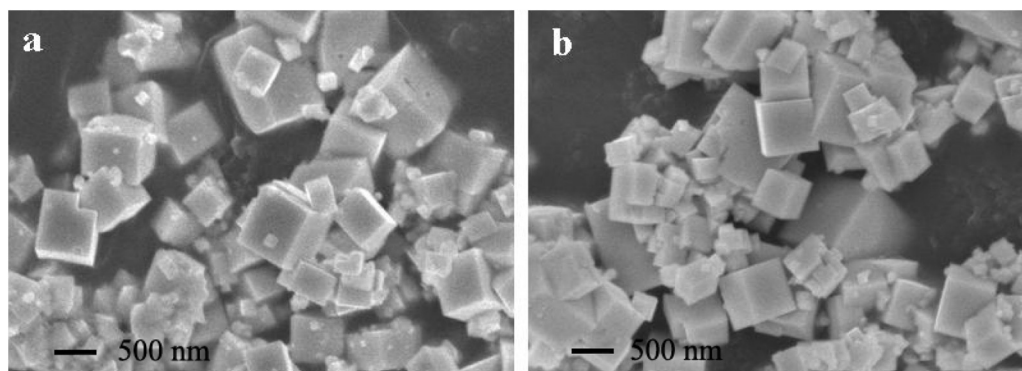

Fig. 2. Representative SEM images of the S-doped NaTaO$_3$ (a) and pure NaTaO$_3$ (b).

Table 1
Crystallographic parameters of S-doped NaTaO$_3$ calculated from XRD data in Fig. 1.

| Sample symbols	a (Å)	b (Å)	c (Å)	β	Volume of cell (Å^3)
S0	3.89597	3.89392	3.89791	90.2255	59.13
S5	3.90156	3.87423	3.91252	90.1017	59.14
S10	3.89949	3.90429	3.89429	90.0936	59.29
S15	3.90075	3.89577	3.90353	90.0494	59.32
S20	3.90175	3.89747	3.90331	90.0267	59.36
S30	3.90661	3.88357	3.91987	90.0162	59.47

3.3. State of Sulfur species doped in NaTaO$_3$.

The chemical states of S atoms incorporated into NaTaO$_3$ were studied by XPS spectra. As shown in Fig. 3, the S-doped NaTaO$_3$ sample (S20) is mainly composed of Na, Ta, O, and S elements and a trace amount of carbon. Quantitative analysis demonstrates that the atomic ratio of S/Ta on the surface of S20 is 3.1%, indicating a much lower doping level in the product than in precursor. And the S/Ta ratio in the product only displays a slight increase (3.5%), in spite of the sharp increase of Na$_2$S$_2$O$_3$ in the precursor (S30). A single peak related to S element is positioned at 161.9 eV in the XPS spectra (inserted at the top of Fig. 3), which is assigned to S^{2-} ions [39], and no S species in cation state are observed [5]. Similar phenomena are also found in S-doped TiO$_2$ system, when S atoms replace O atoms on the TiO$_2$ (1 1 0) surface, the S peak appears at 162 eV [40,41], confirming the anion state of S doped in NaTaO$_3$.

The results can also be confirmed by FTIR analysis. As shown in Fig. 4, S-doped NaTaO$_3$ samples display similar spectra to pure NaTaO$_3$, and no obvious bands related to SO$_3^{2-}$ or SO$_4^{2-}$ groups are observed, indicating the thoroughly elimination of S cations by repetitive washing process during synthesis. The main bands at 500–800 cm^{-1}, asymmetrically centered at 645 cm^{-1}, are attributed to Ta—O stretching and Ta—O—Ta bridging stretching modes [12]. These bands are mainly caused by a totally symmetric combination of coupled Ta—O stretching modes in the chains of tantalum octahedral.

3.4. Photo-absorbance properties.

Fig. 5 shows comparative UV–vis DRS of the pure NaTaO$_3$ and S-doped NaTaO$_3$ powders. The as prepared pure NaTaO$_3$, with monoclinic structure, displays a threshold at 310 nm whose E_g value is estimated to 4 eV. With the increasing doping amount of S, the peak comparative intensity at 232 nm decreases slightly, and the threshold of S-doped NaTaO$_3$ display continuous red shift,
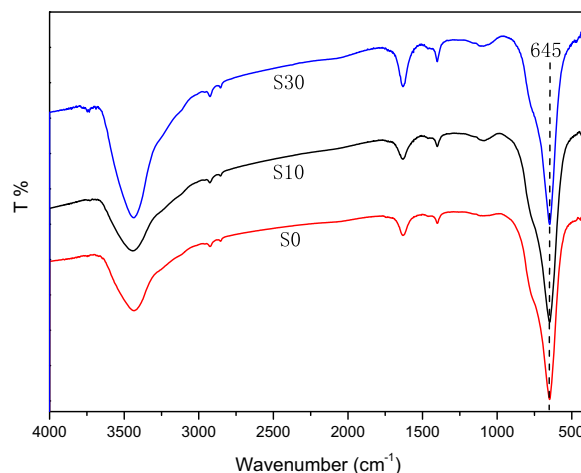
Fig. 4. FTIR spectra of pure NaTaO$_3$ and S-doped NaTaO$_3$ powders.

indicating threatened UV activity and narrowed band gap. For example, the spectrum of S20 displays a main threshold shifted to 317 nm, and an "add-on tail" at the absorption edge of the UV–vis DRS, which extends the light absorption from UV to visible region. The curve of adsorption "tail" of S20 displays several splitting slopes near the threshold, indicating the doping effect of S^{2-} at the local states near the valence band edge, which comes from the overlapping of S 3p orbitals and Ta 5d orbitals and is considered as the main cause for the narrowed band gap of NaTaO$_3$ [30].

3.5. Photocatalytic activities.

The photocatalytic activities of S-doped NaTaO$_3$ samples were evaluated by aqueous degradation of MO under both UV and visible-light irradiation. As shown in Fig. 6a, S-doped NaTaO$_3$ samples display similar photocatalytic degradation rates of MO under
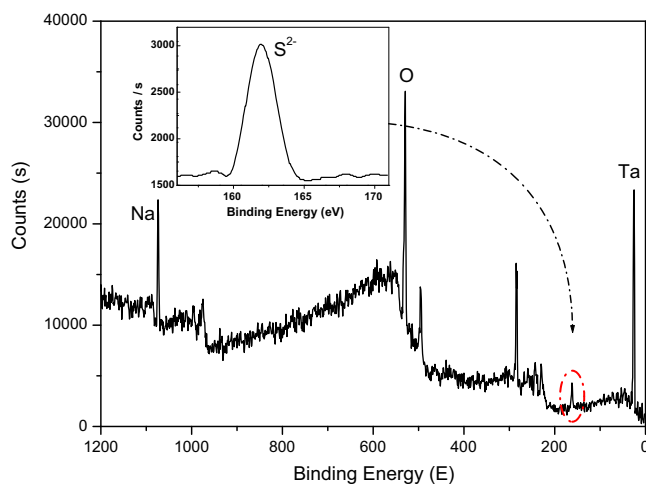
Fig. 3. XPS spectra of the S-doped NaTaO$_3$ powders.
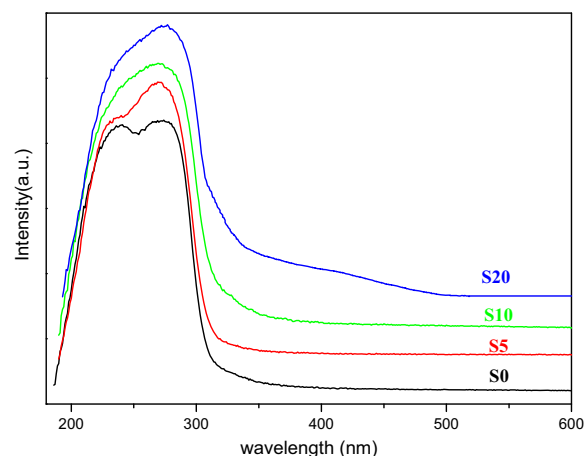
Fig. 5. UV–vis diffuse reflectance spectra of S-doped NaTaO$_3$ and pure NaTaO$_3$ powders.
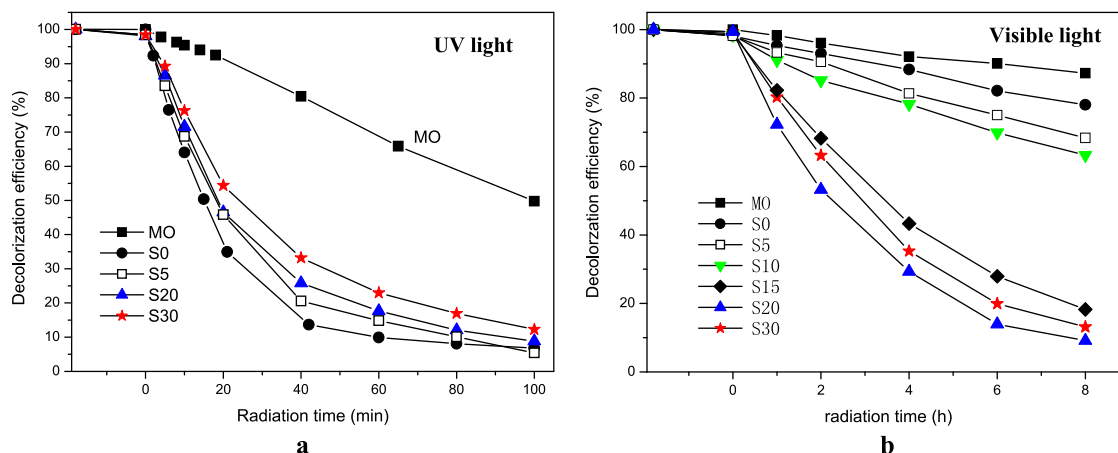
Fig. 6. Photocatalytic degradation of MO (C_o = 20 mg/L) by S-doped NaTaO$_3$ and pure NaTaO$_3$ under UV (a) and visible (b) radiation.

UV light comparing with pure NaTaO$_3$, and no remarkable decay is observed. While, for visible-light irradiation shown in Fig. 6b, the decolorization efficiencies of S-doped NaTaO$_3$ samples are much greater than pure NaTaO$_3$, due to the narrower band gap caused by S doping. And the sample with moderate doping level (S20) displays the best performance, indicating the decay in photocatalytic activity caused by redundant S anion defects doped in NaTaO$_3$ lattice. Fig. 7 shows a plotting of $\ln(A_0/A)$ versus irradiation time (t) for photocatalytic decolorization of MO over S-doped NaTaO$_3$ (S20) and pure NaTaO$_3$. The linearity of kinetic curves reveals that the photocatalytic degradation of MO on the photocatalysts follows pseudo-first-order reaction kinetics. The correlation constant for the fitted line is calculated to be R^2 = 0.9957 and 0.9968, respectively. The apparent rate constant of PCD of MO over S-doped NaTaO$_3$ is much greater (k_1 = 0.306 h^{-1}) than that of pure NaTaO$_3$ (k_1 = 0.029 h^{-1}), which well consists with the XPS and UV–vis DRS results.

GC/MS results reveal the detailed degradation process of MO (whose initial m/z = 304), which has four kinds of intermediates with m/z value at 320, 306, 290, and 276, respectively, at the initial photocatalytic degradation period. With the increasing irradiation time, the m/z value of species in the solution decrease to 256, 242, 212, and 156 gradually, which decreases to the non-toxic inorganic products level, indicating the mineralization of MO.

In order to avoid the sensitization possibility of MO under visible light, phenol is also employed as another target material for the photocatalytic activity test, since it's the typical organic

pollutant in industry waste water and has no absorption in visible region. Fig. 8 displays the photocatalytic degradation rate of phenol (C_o = 20 mg/L) by S-doped NaTaO$_3$ and pure NaTaO$_3$ under visible light. The results show that, similar to MO decolorization, S-doped NaTaO$_3$ samples display obvious visible-light activity than pure NaTaO$_3$, indicating the photocatalytic capability of S-doped NaTaO$_3$ for the degradation of colorless target organics. In the best cases (S20), the degradation efficiency of phenol is 59.8% after irradiated for 8 h, whose corresponding COD removal rate is up to 50.2%, indicating the thoroughly mineralization of phenol on S-doped NaTaO$_3$. These results confirm the directly visible-light photocatalytic activity, other than indirect dye sensitization, of S-doped NaTaO$_3$ catalysts.

Generally, narrowed band gap usually causes reduced photocatalytic stability of perovskite-like structured material. Therefore, the recycling photocatalytic tests were carried out on the best S-doped NaTaO$_3$ sample (S20), by keeping all other parameters constant, where the irradiation time of visible light was fixed on 8 h. In a ten-time recycling test, as shown in Fig. 9, S-doped NaTaO$_3$ displays reliable reusing performance, whose photocatalytic efficiency keeps at a high level and only exists very slight drop due to the loss of photocatalyst during reclaiming process.

3.6. Application factors under solar light.

The above results indicate that anion doping of S species narrows the band gap of NaTaO$_3$ and hence remarkably improves its
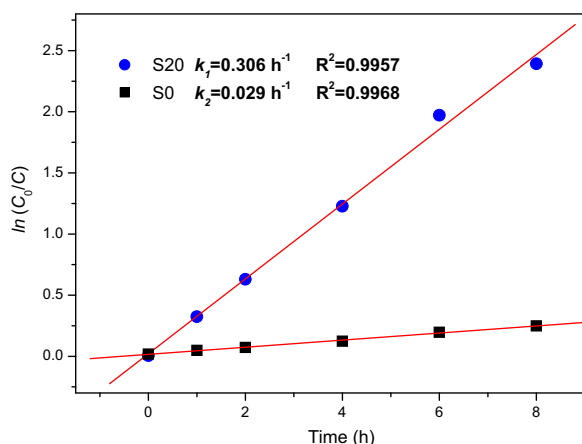

Fig. 7. Kinetic plotting of k_1 over S-doped NaTaO$_3$ (S20) and pure NaTaO$_3$ (S0) fitted from the data in Fig. 6b.
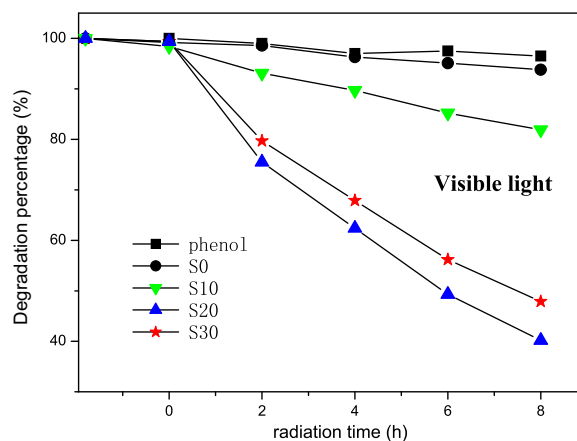

Fig. 8. Photocatalytic degradation of phenol (C_o = 20 mg/L) by S-doped NaTaO$_3$ and pure NaTaO$_3$ under visible light.
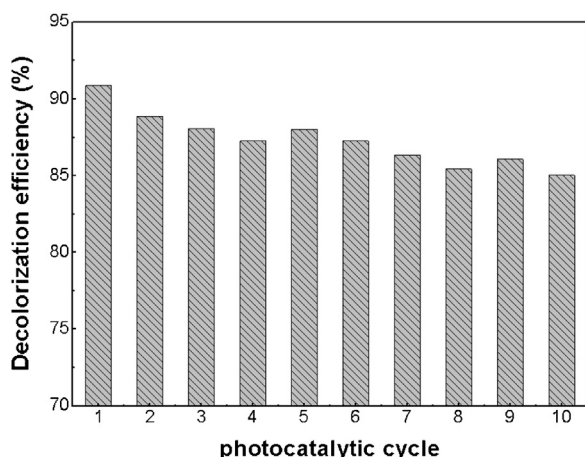
Fig. 9. The recycling photocatalytic performances of S-doped NaTaO$_3$.

Fig. 11. Effects of catalyst dose on photocatalytic performances of S-doped NaTaO$_3$ and pure NaTaO$_3$ under natural solar radiation.

visible-light photocatalytic performance, without obvious decay in UV–light activity at the same time. This is really promising for better solar beam utilizations and further industrial applications of photocatalytic technique. Therefore, in this section, some of the application factors are examined in order to evaluate the practicality of this novel photocatalyst under real solar light, where the irradiation time is added up to 12 h.

Effects of initial pH value. The wastewater from textile industries usually has a wide range of pH values. Generally, the pH of solution is an important parameter in the photocatalytic process. Therefore, comparative experiments were carried out at various initial pH values ranging from 3 to 10 for constant MO concentration (20 mg/L) and catalyst dosage (10 mg/10 mL) under natural solar light. The pH of the solution was adjusted before irradiation and it was not controlled during the course of the reaction. The color removal efficiency of MO as a function of initial pH values is displayed in Fig. 10. The S-doped NaTaO$_3$ (S20) exhibits remarkably higher decolorization efficiency than pure NaTaO$_3$ at all pH values, especially at the region of pH = 4–6. All of the samples display better decolorization efficiency at acidic condition than alkaline condition, due to the improved reductive cleavage and electrostatic adsorption of MO. As known, the ·OH radicals are considered as the most active species during the photocatalytic process, whose amount usually changes with the pH variation of solution, leading to the fluctuation of the photocatalytic degradation rate. The pure NaTaO$_3$ also
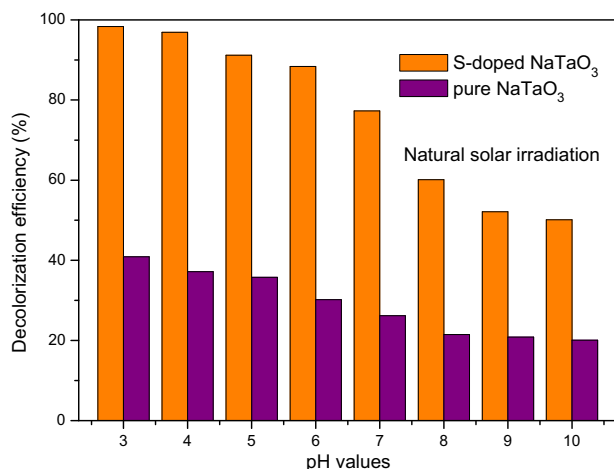
shows slight decolorization efficiency, profited from the small UV fraction of solar irradiation.

Effects of photocatalyst dosage. Since the catalyst dosage was one of the major kinetic factors of photocatalytic reaction, a series of experiments were carried out by varying the amount of samples from 4 to 14 mg/10 mL (C_0 = 20 mg/L, pH = 6). Fig. 11 exhibits the color removal efficiencies of MO as a function of catalyst dosages under natural solar irradiation. Similar to Fig. 9, S-doped NaTaO$_3$ (S20) exhibits superior decolorization efficiencies at all dosages compared with pure NaTaO$_3$, especially when the dosage is relatively high. And all of the samples display a sharp enhanced efficiency by increasing the catalyst dosage at the range of 4∼10 mg/10 mL, attributed to the increased active sites of photocatalysts. Further increasing of the dosage only causes very slight enhancement in the decolorization efficiency, indicating that redundant catalyst shows little benefits in increasing the photocatalytic degradation rate.

3.7. Proposed mechanism

On the basic of the above results, a possible mechanism is proposed to explain the improved photocatalytic activity of S anion-doped NaTaO$_3$. Comparing with conventional orthorhombic CaTiO$_3$ perovskite structure, the lattice of NaTaO$_3$ is distorted into layered perovskite-like structure due to the huge differences in cation size, which enables NaTaO$_3$ with better photoelectrochemical properties and advanced structural tolerance for various dopants [1,2]. Thus, doping of S anions in NaTaO$_3$ lattice is proved to be energetically favorable [30], although the radius of S^{2-} (1.84 Å) is much larger than O^{2-} (1.4 Å) [39], resulting in attractive effects on crystalline structure, electronic structure, and application performance.

As confirmed by XRD results (Fig. 1 and Table 1), the substitution of S anion on the O-site of NaTaO$_3$ will cause slight lattice expansion and structural transition tendency from monoclinic to cubic phase, due to the lager radius of S^{2-}. As known, the arrangement of TaO$_6$ octahedra in cubic phase is an ideal perovskite style, where the bond angle of Ta—O—Ta is 180° [11], leading to the higher mobility of photo-induced charge carriers and better utilization of radiation energy in tantalates [1]. This suggests that the higher activity of S doped-NaTaO$_3$ observed in the present work can be partially promoted by the closer bond angle of Ta—O—Ta to ideal value 180°. In addition, comparing with other anion elements, sulfur anion has the same valence electrons as oxygen, which would not introduce undesirable holes at the top of valance band due to the imbalanced

Fig. 10. Effects of initial pH values on the photocatalytic performances of S-doped NaTaO$_3$ and pure NaTaO$_3$ under natural solar radiation.
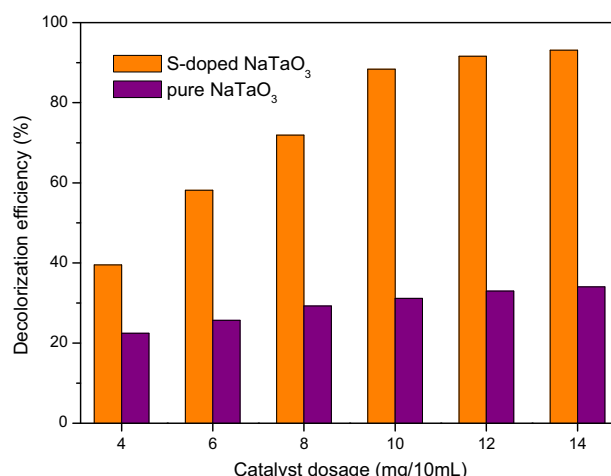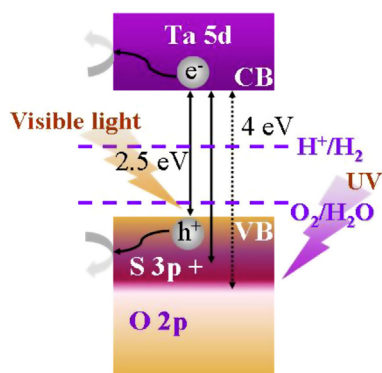
Scheme 1. Proposed mechanism for the improved photocatalytic ativity of S anion-doped $NaTaO_3$.

charges of dopants [30], resulting in the lower recombination rate of photo induced charge carriers and hence improved photocatalytic activities of S anion-doped $NaTaO_3$.

In the strategy of band engineering, S anion doping also display remarkable effect on the red shift of adsorption edge of $NaTaO_3$ observed by UV–vis DRS and photocatalytic tests (Figs. 5–9). The 3p orbital energy of S is higher than O 2p orbitals and is close to the top of the valence band of $NaTaO_3$. In the case of S anion doping, when O is substituted with S, the 3p orbitals of S atom will interact with Ta 5d orbitals, leading to the generation of several discrete midmap bands just above the valence band [30]. This is also confirmed by the splitting slopes near the adsorption threshold shown in Fig. 5, which expands an "add-on tail" into visible light region. It implies that the valence band of $NaTaO_3$ is widened by S anion doping, leading to the narrowed band gap and visible-light activity of S-doped $NaTaO_3$, which is proposed in Scheme 1. It is notable that the experimental E_g values, estimated from the discrete slopes of adsorption edge of S20, are 3.89 eV, 3.48 eV, and 2.53 eV respectively, which dose not consist with the calculation results (3.1 eV) very well [30], due to the different crystalline phase and S doping concentration involved. As the XPS results show, most of the S cations and unreacted S^{2-} species are cleared away by repetitious washing process during synthesis, and only a slight amount of S^{2-} in the precursor is introduced into $NaTaO_3$ lattice successfully, leading to a limited doping level and relevant discount of doping effect. It is understood that further investigations are needed to optimize and enhance the doping efficiency of S anion-doped $NaTaO_3$ system.

Generally, narrowed band gap usually causes improved visible-light photocatalytic performance and corresponding decay in UV–light activity instead. However, in virtue of the higher mobility and better utilization of photo-induced charge carriers, S anion-doped $NaTaO_3$ displays attractive photocatalytic activities under both visible and solar radiation, which is really promising for better solar beam utilization and further applications. Furthermore, the stable layered perovskite-like structure of $NaTaO_3$, in monoclinic or cubic phase, endows S-doped $NaTaO_3$ with superior structural stability and hence reliable recycling photocatalytic performance, which are also crucial for further applications of photocatalytic technique in industry.

4. Conclusions

A novel S-anion doped $NaTaO_3$ photocatalyst was synthesized by a simple hydrothermal process and its photocatalytic activity was evaluated by MO degradation process. As revealed by XPS and FTIR analysis, S species doped into $NaTaO_3$ lattice are purely in anion state. Similar to pure $NaTaO_3$, S-doped $NaTaO_3$ displays well-crystallized nanocubic morphology, according to its natural crystallographic growth habit in hydrothermal system. However,

the crystalline structures and electronic structures of $NaTaO_3$ are notably modified by S anion doping. The XRD results show that, with the increasing doping amount of S species, the unit cell of $NaTaO_3$ expands slightly and a lattice transition tendency from monoclinic to cubic phase is observed, indicating the lower recombination rate of photo induced charge carriers. The UV–vis DRS results reveal that doping of S anions causes obvious red shift and additional "tail" at the absorption edge of $NaTaO_3$, thereby introducing photoactivity at visible-light region. Thus the resultant S-doped $NaTaO_3$ exhibits superior visible-light photocatalytic activity for the degradation of MO, whose decolorization rate constants is much greater ($0.306 \, h^{-1}$) than pure $NaTaO_3$ ($0.029 \, h^{-1}$). Furthermore, its narrowed band gap dose not lead to obvious decay in UV-light activity, due to the lower electron-hole recombination rate caused by S anion doping, resulting in its attractive photocatalytic efficiency under natural solar light. Moreover, S-doped $NaTaO_3$ is photo-stable and broad-pH adaptable, which displays high-level photocatalytic efficiency even after ten-time recycling processes or at various pH conditions. All of these results prove the S anion-doped $NaTaO_3$ to be a promising visible-light photocatalytic candidate among the family of $NaTaO_3$ perovskite-type materials.

Acknowledgment

References

[1] H. Kato, A. Kudo, J. Phys. Chem. B 105 (2001) 4285–4292.
[2] H. Kato, A. Kudo, Catal. Today 78 (2003) 561–569.
[3] J. Wang, S. Yin, M. Komatsu, Q. Zhang, F. Saito, T. Sato, Appl. Catal. B: Environ. 52 (2004) 11–21.
[4] J. Wang, S. Yin, M. Komatsu, Q. Zhang, F. Saito, T. Sato, J. Photochem. Photobiol. A: Chem. 165 (2004) 149–156.
[5] T. Ohno, T. Tsubota, Y. Nakamura, K. Sayama, Appl. Catal. A: Gen. 288 (2005) 74–79.
[6] J.W. Liua, G. Chen, Z.H. Li, Z.G. Zhang, Int. J. Hydrog. Energy 32 (2007) 2269–2272.
[7] P. Kanhere, Y. Tang, J. Zheng, Z. Chen, J. Phys. Chem. Solids 74 (2013) 1708–1713.
[8] O. Vázquez-Cuchillo, R. Gómez, A. Cruz-López, L.M. Torres-Martínez, R. Zanella, F.J. Alejandre Sandoval, K. Del Ángel-Sánchez, J. Photochem. Photobiol. A: Chem. 266 (2013) 6–11.
[9] T. Grewe, K. Meier, H. Tüysüz, Catal. Today 225 (2014) 142–148.
[10] Y. He, Y. Zhu, N. Wu, J. Solid State Chem. 177 (2004) 3868–3872.
[11] C.C. Hu, H. Teng, Appl. Catal. A: Gen. 331 (2007) 44–50.
[12] X. Li, J. Zang, J. Phys. Chem. C 113 (2009) 19411–19418.
[13] M. Zhang, G. Liu, D. Zhang, Y. Chen, S. Wen, S. Ruan, J. Alloys Compd. 602 (2014) 322–325.
[14] Z.H. Li, G. Chen, J.W. Liu, Solid State Commun. 143 (2007) 295–299.
[15] W.H. Lin, C. Cheng, C.C. Hu, H.S. Teng, Appl. Phys. Lett. 89 (2006) 211904.
[16] J. Shi, T. Chen, G. Zhou, Z. Feng, P. Ying, C. Li, Chem. J. Chin. Univ. 28 (2007) 692–695.
[17] P.D. Kanhere, J. Zheng, Z. Chen, J. Phys. Chem. C 115 (2011) 11846–11853.
[18] H. Kato, K. Asakura, A. Kudo, J. Am. Chem. Soc. 125 (2003) 3082–3089.
[19] D.G. Porob, P.A. Maggard, J. Solid State Chem. 179 (2006) 1727–1732.
[20] X. Li, J. Zang, Catal. Commun. 12 (2011) 1380–1383.
[21] L.M. Torres-Martínez, A. Cruz-López, I. Juárez-Ramírez, M.E. Meza-de la Rosa, J. Hazard. Mater. 165 (2009) 774–779.
[22] L.M. Torres-Martínez, R. Gómez, O. Vázquez-Cuchillo, I. Juárez-Ramírez, A. Cruz-López, F.J. Alejandre-Sandova, Catal. Commun. 12 (2010) 268–272.
[23] P. Kanhere, J. Nisar, Y. Tang, B. Pathak, R. Ahuja, J. Zheng, Z. Chen, J. Phys. Chem. C 116 (2012) 22767–22773.
[24] D.R. Liu, C.D. Wei, B. Xue, X.G. Zhang, Y.S. Jiang, J. Hazard. Mater. 182 (2010) 50–54.
[25] X. Wang, G. Liu, Z.G. Chen, F. Li, G.Q. Lu, H.M. Cheng, Chem. Lett. 38 (2009) 214–215.
[26] H.B. Fu, S.C. Zhang, L.W. Zhang, Y.F. Zhu, Mater. Res. Bull. 43 (2008) 864–872.
[27] Y.X. Zhao, D.R. Liu, F.F. Li, D.F. Yang, Y.S. Jiang, Powder Technol. 214 (2011) 155–160.
[28] D.R. Liu, Y.S. Jiang, G.M. Gao, Chemosphere 83 (2011) 1546–1552.
[29] Xin Zhou, Jingying Shi, Can Li, J. Phys. Chem. C 115 (2011) 8305–8311.
[30] B. Wang, P.D. Kanhere, Z. Chen, J. Nisar, B. Pathak, R. Ahuja, J. Phys. Chem. C 117 (2013) 22518–22524.
[31] R. Asahi, T. Morikawa, T. Ohwaki, K. Aoki, Y. Taga, Science 293 (2001) 269–271.

[32] T. Ohnoa, M. Akiyoshi, T. Umebayashi, K. Asai, T. Mitsui, M. Matsumura, Appl. Catal. A: Gen. 265 (2004) 115–121.
[33] T. Ohno, N. Murakami, T. Tsubota, H. Nishimura, Appl. Catal. A: Gen. 349 (2008) 70–75.
[34] V.M. Menéndez-Flores, D.W. Bahnemanna, T. Ohno, Appl. Catal. B: Environ. 103 (2011) 99–108.
[35] K. Kondoa, N. Murakamia, C. Yea, T. Tsubotaa, T. Ohno, Appl. Catal. B: Environ. 142–143 (2013) 362–367.
[36] Y. Lee, T. Watanabe, T. Takata, J.N. Kondo, M. Hara, M. Yoshimura, K. Domen, Chem. Mater. 17 (2005) 2422–2426.
[37] J.S. Xu, D.F. Xue, C.L. Yan, Mater. Lett. 59 (2005) 2920–2922.
[38] O. Vázquez-Cuchillo, A. Manzo-Robledo, R. Zanella, N. Elizondo-Villareal, A. Cruz-López, Ultrason. Sonochem. 20 (2013) 498–501.
[39] J. Wang, H. Li, H. Li, S. Yin, T. Sato, Solid State Sci. 11 (2009) 182–188.
[40] T. Umebayashi, T. Yamaki, H. Itoh, K. Asai, Appl. Phys. Lett. 81 (2002) 454–456.
[41] E.L.D. Hebenstreit, W. Hebenstreit, H. Geisler, S.N. Thornburg, C.A. Ventrice, D.A. Hite Jr., P.T. Sprunger, U. Diebold, Phys. Rev. B 64 (2001) 115418.